Computer simulations of the interactions of the (012) and (001) surfaces of jarosite with Al, Cd, Cu^{2+} and Zn

Karen A. Hudson-Edwards[1*] and Kate Wright[2]

[1] Department of Earth and Planetary Sciences, Birkbeck, University of London, Malet Street, London, WC1E 7HX, UK. *Corresponding author. Tel: +44-(0)207-679-7715; Fax: +44-(0)207-679-2867; Email: k.hudson-edwards@bbk.ac.uk.

[2] Nanochemistry Research Institute, Department of Chemistry, Curtin University of Technology, GPO Box U1987, Perth, WA 6845, Australia.

Accepted version for publication in: *Geochimica et Cosmochimica Acta*

Keywords: jarosite; surface; atomistic simulation; impurities; aluminum; cadmium; copper; zinc

Abstract

Jarosite is an important mineral on Earth and possibly, on Mars, where it controls the mobility of iron, sulfate and potentially toxic metals. Atomistic simulations have been used to study the incorporation of Al^{3+}, and the M^{2+} impurities Cd, Cu and Zn, in the (012) and (001) surfaces of jarosite. The calculations show that the incorporation of Al on an Fe site is favorable on all surfaces in which terminal Fe ions are exposed, and especially on the (001) $[Fe_3(OH)_3]^{6+}$ surface. Incorporation of Cd, Cu or Zn on a K site balanced by a K vacancy is predicted to stabilize the surfaces, but calculated endothermic solution energies and the high degree of distortion of the surfaces following incorporation suggest that these substitutions will be limited. The calculations also suggest that incorporation of Cd, Cu and Zn on an Fe site balanced by an OH vacancy, or by coupled substitution on both K and Fe sites, is unfavorable, although this might be compensated for by growth of a new layer of jarosite or goethite, as predicted for bulk jarosite. The results of the simulations show that surface structure will exert an influence on uptake of impurities in the order Cu > Cd > Zn, with the most favorable surfaces for incorporation being (012) $[KFe(OH)_4]^0$ and (001) $[Fe_3(OH)_3]^{6+}$.

1. INTRODUCTION

Excessive concentrations of toxic elements in soils and groundwater threaten human and ecosystem health. These threats arise through leakages, spills and natural weathering. The toxic elements can be immobilized and their bioavailability reduced by the formation of new minerals that incorporate them, or by their uptake onto pre-existing mineral surfaces. An understanding of the mechanisms by which minerals take up toxic elements will inform risk assessments and underpin the development of effective remediation systems.

Many studies have demonstrated that jarosite minerals can host potentially toxic elements (e.g., Dutrizac and Dinardo, 1983; Dutrizac, 1984; Scott, 1987). Jarosite-group minerals are members of the isostructural jarosite-alunite group of minerals that has a general formula of $AB_3(TO_4)_2(OH)_6$. The A and B sites in jarosite can be filled by potentially toxic elements including Al, Cd, Cu and Zn. Jarosite-group minerals occur in acid sulfate soils (Welch et al., 2007), acid mine wastes (Jambor, 1994; Hudson-Edwards et al., 1999), saline lakes (Alpers et al., 1992; Benison et al., 2007) and hypogene systems (Martínez-Frias et al., 2004). They are used in metallurgical processes to remove unwanted iron and improve the purity and grade of metal concentrates (Jiang and Lawson, 2006), form undesirable scales in autoclaves during ore processing (Timms et al., 2009), and have been employed as pigments in ancient artwork (Wallert, 1995). Mössbauer spectroscopic data have also been used to infer the existence of jarosite on Mars, suggesting that water and possibly, life, once existed on this planet's surface (Klingelhöfer et al., 2004). An understanding of how jarosite-group minerals take up potentially toxic elements will therefore give a better understanding of the cycling of these elements in these widespread environments.

Atomistic computer simulation studies have increasingly been used over the last three decades to complement experimental and natural studies by giving detailed information on the structure and properties of solids at the atomic level (Catlow, 2003). This information can help to interpret

experimental data and make predictions on parameters that are difficult to quantify. For example, computational simulations on K-jarosite have shown that there is selective dissolution of the A- and T-sites (Smith et al., 2006b), and that Cd, Cu^{2+} and Zn can be incorporated into the bulk structure by substitution for Fe^{3+} on the B site via solution reactions with oxides leading to the formation of goethite (Smith et al., 2006a). In order to understand toxic element uptake mechanisms, however, it is crucial to understand the nature of the mineral surface, since all important reactions take place here (e.g., Gräfe et al., 2008). In this paper, we have carried out atomistic simulations aimed at understanding the mechanisms of incorporation of Al, Cd, Cu^{2+} and Zn in K-jarosite and the influence of surface structure on uptake.

2. COMPUTATIONAL METHODS

2.1. Interatomic potentials and development of the jarosite model

For this study we have used classical atomistic simulation methods, which are based on the Born model of solids that uses interatomic potentials to describe the energy of a system in terms of the atomic co-ordinates. For ionic solids, the dominant term is the long-range Coulomb interaction, with short-range repulsive forces provided by the overlap of nearest neighbor electron clouds. These short-range interactions may be two-, three- or many-body and may describe both bonded and non-bonded interactions. The variable parameters of the potentials are generally obtained by empirical fitting to experimental data, including cell parameters, elastic constants and spectroscopic data (Gale and Rohl, 2003).

All calculations reported here were carried out with the GULP code (Gale and Rohl, 2003) using standard energy minimization schemes in which the energy of the system is calculated with respect to all atomic co-ordinates. Equilibrium positions of the ions are evaluated by minimizing the

lattice energy until all forces acting on the crystal are removed. We describe non-bonded 2-body interactions using a Buckingham potential of the form:

$$U(r_{ij}) = A \exp\left(-\frac{r_{ij}}{\rho}\right) - \frac{C}{r_{ij}^6}, \quad (1)$$

where the parameter A represents the repulsion between two ions *i* and *j* separated by a distance *r*, ρ is related to the size and hardness of the ions and C is the term included to model dispersion (Gale and Rohl, 2003). For bonded interactions involving OH^- and SO_4^{2-} the Morse potential is used:

$$U(r_{ij}) = D_{ij}\left(1 - \exp\left[-\alpha\left(r - r_0\right)\right]\right)^2 \quad (2)$$

In this equation, D is the bond dissociation energy, r_0 is the equilibrium bond distance and α is a function of the slope of the potential energy well that is taken from spectroscopic data (Catlow and Mackrodt, 1982). We use a 3-body term to simulate the directionality of the bonding of S in a tetrahedral environment, since this will be partly covalent, and this is represented by:

$$U(\theta_{ijk}) = \frac{1}{2} k_{ijk}(\theta_{ijk} - \theta_0)^2 \quad (3)$$

where k is the force constant, Θ_{ijk} is the bond angle acting between ions *i*, *j* and k, and Θ is the equilibrium bond angle.

The potential parameter set used in this study is based on that derived from jarosite and described in Smith et al. (2006a, b) but with some improvements. For this study, a simultaneous fit was performed for jarosite, allowing the Buckingham A and ρ parameters for K-O1, K-O2, Fe-O1 and Fe-O2 to vary while all parameters for the OH- and SO_4^{2-} interactions were kept fixed. The structure of jarosite was included as observables in the fitting procedure. The sulfate phase of each of the impurity ions was modeled to provide O1-M *A* and ρ parameters and the A parameters then scaled according to the magnitude of the charges, to give values for O2-M. The revised set of potential parameters is given in Table 1.

2.2. Surface calculations

Surface structures are modeled using a two-dimensional periodically repeating simulation cell, divided into two regions. Region 1 contains those ions that effectively make up the surface, and region 2 represents the bulk crystal. All atoms within Region 1 are relaxed to their equilibrium positions on the surface while those in Region 2 are held fixed at their relaxed, bulk co-ordinates. The depth of the regions must be sufficient that all surface relaxations are accommodated in Region 1 and no strain acts upon the interface between the two. Region 2 must be large enough to exert the correct bulk potential on Region 1.

Surface energies were calculated for perfect and defective surfaces. The surface energy (γ) is defined as the work done to cleave a surface from the bulk:

$$\gamma = U_{Surf} - U_{Bulk} / A \quad (4)$$

where U_{Surf} is the energy of the surface block (in J m^{-2}), U_{Bulk} is the energy of that same block in the bulk material (in J m^{-2}) and A is the surface area. The lower the surface energy, the more stable the surface will be and thus the more readily it will be expressed in the crystal morphology.

2.3. Substitution of Al, Cd, Cu and Zn into jarosite surfaces

Incorporation of the impurity ions Al^{3+}, Cd^{2+}, Cu^{2+} and Zn^{2+} onto the perfect surfaces via four mechanisms was investigated. The mechanisms involved substituting the ions at the K and Fe sites and in almost all cases, introducing other defects in order to maintain charge neutrality. The sets of possible

defect combinations for the metal impurities are:

(i) substitution at a K site charge balanced by a K vacancy $M_K^{\bullet} + V_K^{/}$;

(ii) substitution at Fe sites charge-balanced by (OH) vacancies $M_{Fe}^{/} + V_{OH}^{\bullet}$;

(iii) coupled substitution at K and Fe sites $M_K^{\bullet} + M_{Fe}^{/}$; and

(iv) straight substitution of Al for Fe Al_{Fe}^{x}

We use Kröger-Vink defect notation (Kröger, 1972) to describe the substitutions. In this notation, the subscript denotes the site of the impurity and the superscript the charge, where x is neutral, ' is negative and $^{\bullet}$ is positive. Thus in the above, $M_K^{\bullet}$ represents an impurity at the K site and is positively charged, $V_K^{/}$ is a negatively charged K vacancy, $M_{Fe}^{/}$ is a negatively charged substitution and $V_{OH}^{\bullet}$ is a positively charged vacancy with a net charge of one, and Al_{Fe}^{x} is a neutral substitution of Fe at the Al site.

The relative effects of different impurity/vacancy defect complexes on the structure and stability of surfaces can be assessed by optimizing the surface ion positions and calculating substitution (U_{Subs}) and defective surface energies (γ_{eff}) relative to the pure surface. U_{Subs} is calculated as the difference between the relaxed perfect surface and the defective surface cells:

$$U_{Subs}\ \text{surface} = U_{Tot}\ \text{defective surface} - U_{Tot}\ \text{pure surface} \quad (5)$$

The magnitude change in surface energy on the introduction of the impurities is defined as the effective surface energy (γ_{eff}, in J m^{-2}), and is calculated as follows:

$$\gamma_{eff} = \gamma + (U_{subs}/A) \quad (6)$$

where U_{Subs}, in this case, is the energy cost of adding the defect to the surface.

The incorporation of impurity metal cations into jarosite surfaces in the natural environment is pH dependent, occurs at ambient temperature, and in the presence of an aqueous fluid. Although the data presented so far in this paper are limited to vacuum conditions at zero Kelvin and at the point of zero charge of the jarosite surface, it is still possible to assess the influence of a solvent on the incorporation of impurities into jarosite by determining their segregation energies in the surfaces relative to solution. For this:

$$\text{Solution } U_{Sol} = U_{Subs} \text{ surface} - U_{Solv\text{-}exchange} \quad (7)$$

Here, $U_{Solv\text{-}exchange}$ is the solvation exchange reaction, and is defined as:

$$M1_{aq} + M2_{surface} \Leftrightarrow M1_{surface} + M2_{aq} \quad (8)$$

where M1 exchanges with M2 between the surface and the solution. The calculated U_{Sol} values then give an indication of whether the impurities prefer to substitute in the jarosite surface or stay in solution.

The program GDIS (Fleming and Rohl, 2005) was used to visualize the jarosite model, create surfaces, view relaxed and substituted surfaces, calculate bond angles and distances and view crystal morphologies with and without defect substitutions. Substitutions were made at K and/or Fe sites in the uppermost layer of the (012) and (001) surfaces of jarosite, depending on the stoichiometry of the exposed terminating layer. Calculations were performed on a 3×2 surface for all but the 001-S1 surface (see section 3.1 below), for which a 4×2 surface was used. Where more than one defect was

present in the substitution complex, the individual components were placed in adjacent sites (bound) and then at sites separated by a minimum of 8 Å (unbound). The relative effect of incorporating bound defect complexes on the structure and stability of surfaces is assessed by calculating the binding energy (U_{Bind}), as follows:

$$U_{Bind} = U_{Subs}\ \text{bound} - U_{Subs}\ \text{unbound} \quad (9)$$

3. RESULTS AND DISCUSSION

3.1. Bulk structure and pure surfaces

The alunite supergroup comprises isostructural minerals with the general formula $AB_3(TO_4)_2(OH)_6$. In the formula, A represents cations with a coordination number >= 9, B represents cations with slightly distorted octahedral (O) coordination, and T represents cations with tetrahedral (T) coordination (Jambor, 1999; Hawthorne et al., 2000). In ideal jarosite [$KFe_3(SO_4)_2(OH)_6$], the B site cation is Fe(III), the A site is occupied by K^+ in 12-fold coordination, and the T site is filled with sulfate (SO_4^{2-}) (Kubisz, 1964, 1970; Brophy and Sheridan, 1965; Dutrizac and Kaiman, 1976). Each of the octahedra has four bridging hydroxyl groups in a plane, and sulfate oxygens at the apices. The structure of jarosite has $R\bar{3}$m symmetry, with the metal B-site ions located in slightly distorted octahedral sites. Three of the tetrahedral sulfate oxygens are coordinated to Fe, reducing the symmetry of the SO_4^{2-} tetrahedra from T_d to C_{3V}. The Fe ions are jointed by the SO_4^{2-} tetrahedra and by the network of di-hydroxyl bridges to form sheets separated by the uncoordinated sulfate oxygens and the A-site K cation (Jambor, 1999; Becker and Gasharova, 2001).

The bulk structure of jarosite, produced using the potential parameters listed in Table 1, has

calculated cell parameters and bond lengths that are within 0.1% of the experimental values and maintain the correct *a/c* ratio, as shown in Table 2. All bond lengths and angles are also in good agreement, except the S-O distance, which is 4.3% shorter than reported by Menchetti and Sabelli (1976) (Table 2), and is discussed further below. No elastic constant experimental data are available with which to compare our results, although we note that the calculated value for the bulk and shear moduli are K_{RVH} = 60.76 GPa and G_{RVH} =45.17 GPa, almost identical to those calculated by Majzlan et al (2006) using the model of Becker and Gasharova (2001).

Natural and synthetic jarosite crystals are predominantly terminated by the most stable (012) faces and hence these have been most extensively studied (Becker and Gasharova, 2001; Gasharova et al., 2005; Smith et al., 2006b, Wright et al., 2008). The optimized bulk structure of jarosite was cleaved at two depths to produce two non-charged (012) surfaces, designated 012-S1 and 012-S2, which were then relaxed. Convergence of the surface energy was achieved for a simulation cell with equal numbers of layers in R1 and R2 and a total depth of 30 Å. 012-S1 comprises neutral sub-layers of composition $[Fe_2(SO_4)_2(OH)_2]^0$, and 012-S2, neutral sub-layers of composition $[KFe(OH)_4]^0$. On relaxation, 012-S2 undergoes considerable reconstruction, with rotation of OH groups and distortion of the SO_4^{2-} tetrahedron. The K^+ ions move upwards while the Fe^{3+} moves down into the surface by over 1 Å. This leads to an increase and opening up of the surface and an increase in the accessible surface area, making the K^+ and SO_4^{2-} ions more susceptible to leaching in an aqueous environment (Smith et al., 2006b). The degree of relaxation in S1 is much less, with the SO_4^{2-} group moving down slightly. Computed surface energies are 1.19 J m^{-2} and 0.99 J m^{-2} for 012-S1 and 012-S2, respectively (Table 3).

Becker and Gasharova (2001) described triangular (001) faces on synthetic jarosite crystals, but showed that most of these disappeared in favor of the (012) faces in larger crystals. Two other charged surfaces can be produced by cleaving the (001) surface at two different depths above the OH apices of the Fe^{3+} octahedra and above the Fe^{3+} ions. All three surfaces are, in the notation of Tasker (Tasker, 1979), type III surfaces. Type I surfaces are composed of charge neutral units for all possible surface

cuts, while Type II surfaces can only be cut at particular depths to produce a non-dipolar surface. Type III surfaces, however, cannot be cleaved to produce a charge neutral surface and therefore must be reconstructued to remove the dipole. In nature, such reconstruction comes about by large re-organisation of the surface layers by, the formation of defects, or by hydroxylation reactions. GDIS was used to create three (001) surfaces, designated 001-S1, 001-S2 and 001-S3. The dipoles were removed from these surfaces by translating one K^+ ion, one Fe^{3+} ion, and three Fe^{3+} ions in a line, respectively, from the top to the bottom of the slab or vice versa. Surfaces 001-S1, 001-S2 and 001-S3 comprise sub-layers of compositions $[K(SO_4)_2]^{3-}$, $[Fe_5(OH)_{12}]^{3+}$ and $[Fe_3(OH)_3]^{6+}$ (Table 3). Upon relaxation of the 001-S1 surface, the K^+ ions move between 2.5 and 3 Å above the surface, and the SO_4 tetrahedra rotate slightly towards the central K^+ ion. The 001-S2 surface reconstructs to a considerable degree following relaxation, with rotation and movement upwards of half of the Fe^{3+}, K^+ and OH^- ions, and rotation of the SO_4 groups on the outside of the simulated cell. The 001-S3 surface also undergoes extensive reconstruction after relaxation. The surface OH^- ions rotate by almost 180º and move upwards, two-thirds of the Fe^{3+} ions sink into the surface by 1.7 Å, half of the K^+ ions move upwards by 3.7 Å and half of the $(SO_4)^{2-}$ ions rotate and move upwards. Computed surface energies are 0.43, 1.01 and 1.08 J m^{-2} for 001-S1, 001-S2 and 001-S3, respectively (Table 3).

To determine whether our short S-O distance influenced surface energies, we used our original jarosite model (Smith et al., 2006a, b) to create the same (012) and (001) surfaces reported above. In all cases, the relaxed surface energies were the same as those reported in Table 3, suggesting that S-O bond lengths do not heavily influence the surface energies.

3.2. Al incorporation

The substitution of Al for Fe site (mechanism iv, section 2.3) is the most straightforward of all the impurities considered, as it is charge neutral. Substitution on both (012) surfaces leads to a reduction in

the energy of the surface block (Table 4), i.e. give negative values for U_{Subs} (Table 5). The influence of the defect on the structure is similar for both surfaces. On the 012-S1 surface Fe and Al are coordinated by three hydroxyl oxygens (O2) and two sulfate oxygens (O1). The Al-O1 distance is reduced by around 8%, while for O2 is around 4% (Table 6). On the 012-S2 surface, Fe and Al are still in 5-fold coordination, but there are four hydroxyl and only one sulfate oxygen. As before, decrease in Al-O1 (10%) is greater than Al-O2 (4%) (Table 6).

No Fe is present at the termination of the 001-S1 surface, but there are two distinct sites on 001-S2 and three on 001-S3. On 001-S2 (Fig. 1), one site is 5-fold co-ordinated and the other 6-fold; and it is the former which is more favorable for Al substitution by 14.5 kJ mol^{-1}. This surface shows the most pronounced reduction in surface energy (15%) upon substitution of the four surfaces in which this occurs (Table 4). For 001-S3, Fe (and hence Al) can be in either a 4-, 5- or 6-fold site. Of these, the 5-fold site surrounded by three hydroxyl and two sulfate oxygens has the lowest substitution energy (Table 5). Al at this site is more than 96.5 kJ mol^{-1} lower in energy that the next nearest value, which is for Al at a 4-fold site. Changes in bond lengths follow much the same trend as in the (012) surfaces, with Al-O1 distances increasing between 12-14% and Al-O2 increases being much smaller at around 5% (Table 6).

Al could also be incorporated at the K site, charge balanced by two K vacancies, but this leads to a large disruption of the surface and a substantial change to the surface stoichiometry on the scale of the cells used in this study. Thus it is much more likely that Al will be incorporated via substitution at the Fe site.

3.3. M^{2+} substitutions

Substitution of M^{2+} ions can take place by three defect mechanisms, (i) $M_K^{\bullet} + V_K^{/}$, (ii) $M_{Fe}^{/} + V_{OH}^{\bullet}$ and

(iii) $M'_{Fe} + M^{\bullet}_{K}$, as described in section 2.3. Calculated values of U_{Subs} for these defect complexes are made up of contributions from the impurity substitution(s) plus the formation energies of the associated charge-compensation defects. Absolute values of these energies have no meaning because there are fewer ions in the defective block than in the pure, but a comparison of substitution energies for different configurations of the same defect can tell us which configuration is likely to be most stable, and if there is any defect binding.

3.3.1. $M^{\bullet}_{K} + V'_{K}$

K^+ ions are only present in the 012-S2, 001-S1 and 001-S3 surface terminations and so only these are considered. The *relative* values of U_{Subs} for the $M^{\bullet}_{K} + V'_{K}$ defect on 012-S2 tell us that Cu has the greatest effect on the energy of the simulation block and Cd the least (Table 5). This can be understood by considering the disruption to the surface structure induced by the defects. Unbound substitution of these ions results in movement upwards and rotation of many of the OH^- groups around the K vacancy so that they point upwards with H atoms lying above the surface. The M^{2+} impurity sinks slightly into the surface while the underlying $(SO_4)^{2-}$ groups rotate towards it, accompanied by a small upward movement of the K ions adjacent to the vacancy and impurity. This reconstruction leads to a reduction in the 012-S2 surface energy with the largest reduction being for Cu, followed by Zn, and then Cd (Table 4). Cu likely has the greatest effect because it is the smallest of the three impurity ions considered (Cu 0.73 Å < Zn 0.74 Å < Cd 0.95 Å for co-ordination numbers (CN) of 6 and substitution on B-sites; Shannon, 1976), and it is smaller than the K ion it is replacing (1.64 Å; Shannon, 1976). In all cases the effective surface energy is more favorable when the impurity/vacancy pair is bound as shown in Table 4. These surfaces will therefore be stabilized by the presence of M^{2+} impurities and hence more readily expressed in the external crystal morphology.

On the 001-S1 and 001-S3 surfaces, the impurities again sink into the surface and cause the

adjacent $(SO_4)^{2-}$ groups to rotate inwards (Fig. 1) with O1-M distances of 2.06Å (Cu), 2.07Å (Zn) and 2.17Å (Cd) for 001-S1 and 2.09Å (Cu), 2.09Å (Zn) and 2.11Å (Cd) for 001-S3. For both 001-S2 and 001-S3, substitution and effective surface energies follow the same trend as for the 012-S2 surface, but 001-S2 shows only a weak propensity for the vacancy and substitution to bind together (Tables 4, 5, 7), and 001-S3 shows unfavorable binding energies (Table 7).

3.3.2 $M_K^{\bullet} + M_{Fe}^{/}$

The coupled substitution energy of metals at K and Fe sites was calculated for the 012-S2 and 001-S3 surfaces. Relative substitution energies for same species substitutions again show general trend U_{Subs} = Cu < Zn < Cd (Table 5), although binding energies are now positive, except in the case of Cd in 012-S2, which is slightly negative (Table 7). All combination of the three impurities lead to an increase in effective surface energy (Table 4), suggesting that the surfaces are destabilized by these substitutions. There is minimal distortion of the 012-S2 surface, with the ion substituting for K moving towards that substituting for the Fe ion, and very slight rotation of the other ions towards the impurity ions (Fig. 1). The 001-S3 surface undergoes more distortion; the impurity at the Fe site sinks into the surface by c. 1 Å while the other ions rotate towards the impurities.

$M_{Fe}^{/} + V_{OH}^{\bullet}$

Bound and unbound substitutions of Cd, Cu and Zn for Fe with an OH vacancy were calculated for all surface termination except 001-S1, which does not contain Fe. Of these, the 012-S1 surface undergoes the most distortion after substitution: the impurity ion substituting for Fe rises to the surface by c. 2.5 Å, and the $(SO_4)^{2-}$ and $(OH)^{-}$ groups surrounding the impurity rotate towards it (Fig. 1). After substitution on the 012-S2 surface, the $(OH)^{-}$ group nearest the impurity rotates so that it protrudes upwards from the surface. The surrounding ions move very slightly towards the substituting impurity

on the 001-S2 surface, and on the 001-S3 surface, the impurity that replaces Fe moves laterally by almost 2 Å and sinks slightly (< 1 Å) into the surface. In all of these cases, the distortions are so great that the surfaces are likely destabilised.

Increases in γ_{eff} are of the order of 50-60% over the pure surface for (012) (Table 4), which will make these surfaces highly unstable and facilitate rapid growth. The increase is even greater for the (001) surfaces (Table 4). This suggests that incorporation by this mechanism is unlikely. If the energy barrier is overcome such that substitutions do occur, then the values of U_{Subs} indicate differences in the way that each of the (001) and (012) surfaces accommodate this defect complex. For 012-S1, 001-S2 and 001-S3, both unbound and bound defects are favored in the order Cu > Zn > Cd but for 012-S2 the trend is for Cd > Cu > Zn (bound) and Zn > Cd > Cu (unbound) (Table 5). For the four surfaces, incorporation is favored in the order 012-S2 > 012-S1 > 001-S3 > 001-S2 (Table 5).

3.3. Incorporation of metal cations in jarosite surfaces via solution reaction

Possible solution reactions leading to impurity incorporation via the four mechanisms considered are shown in Table 8. U_{Sol} values (Table 9) were calculated using values of molar Gibbs energy of hydration ($\Delta_{hyd}G$) from Marcus (1991). We make the assumption of infinite dilution when using the data of Marcus (1991). Also, the values of Marcus (1991) are reported for T=298.15K, which is different than the 0K used in our calculations. However, the effects of temperature in solution are far greater than those on the energy of in the crystal, so we assume that the effects of temperature on the entropy contribution and on heat capacity are negligible. It should be noted that the calculated U_{Sol} energies cannot be compared for the different impurity ions, because their absolute values are dependent on the value used for hydration, which vary depending on how they were obtained. U_{Sol} energies are therefore compared for the same ion on different surfaces.

Values of U_{Sol} are negative for all of the Al_{Fe}^{x} substitutions (Table 9), suggesting that it is favorable for Al to segregate from solution to the jarosite surface. In these reactions, the surfaces are favored in the order 001-S3 > 012-S2 > 001-S2 > 012-S1.

For the remaining substitutions, values of U_{Sol} are positive for all but the $Cu_K^{\bullet} + V_K^{/}$ substitutions. This suggests that for Reaction 2 (Table 8), the impurity metal cations would prefer to remain in solution rather than exchanging with Fe or K on the jarosite surfaces (except for $Cu^{2+}_{(aq)}$, which shows a preference for segregating to the surface). U_{Sol} values are strongly positive for the $M_{Fe}^{/} + V_{OH}^{\bullet}$ substitutions, with Cu > Zn > Cd and bound > unbound, and 012-S1 generally having the highest and 001-S3, the lowest values. For the $M_K^{\bullet} + V_K^{/}$ substitutions, U_{Sol} values decrease in the order 001-S1 > 001-S3 > 012-S2, Cu > Zn > Cd for 001-S1 and 001-S3, Zn > Cd > Cu for 012-S2, and bound > unbound. Values of U_{Sol} for the $M_K^{\bullet} + M_{Fe}^{/}$ substitutions on the 001-S3 surface are higher than those on the 012-S2 surface, higher for bound compared to unbound substitutions, and decrease in the order Zn > Cu > Cd, except for the unbound 012-S2 substitutions, for which Zn > Cd > Cu.

3.4. Implications for incorporation of impurities in jarosite in natural and engineered environments

Our calculated data are limited because we have not considered the possible presence of water on the surface of jarosite, the incorporation of hydronium (H_3O^+) for K in the jarosite structure (which could make K-site substitutions less favorable), and the fact that the uptake of contaminants on mineral surfaces in real systems depends on ambient environmental conditions (temperature, pH, flow conditions, fluid composition, etc.). Therefore, our results place upper limits on the energetics of these processes, and provide guides for the most likely reactions. Although our model is simple, it does show that the structure and chemistry of the jarosite surface will influence sorption and exchange behavior.

The calculations suggest that the substitution of Al for Fe will stabilize the 012-S1, 012-S2, 001-S2 and 001-S3 surfaces (Table 4, 5), and that is favorable for Al to segregate from solution to the jarosite surface (Table 9). The incorporation of Al for Fe in natural jarosite-group minerals has been reported (Brophy et al., 1962; Alpers et al., 1992), but this may be limited, as it is not known whether a naturally-occurring full solid solution series or a miscibility gap exists between jarosite and alunite [$KAl_3(SO_4)_2(OH)_6$] end-members (Stoffregen et al., 2000). Furthermore, Al hydrolysis takes place at a pH value of 5.0 (Nordstrom and May, 1996), which is above the stable pH range for jarosite (Baron and Palmer, 1996).

In terms of the 2+ cations, incorporation of Cu is most favored, followed by Zn and Cd for the defect mechanisms investigated. This order reflects the relative sizes of the radii of the cations (Cu < Zn < Cd; Shannon, 1976), and also agrees with Dutrizac et al. (1996), who determined the order of incorporation of 2+ metals by jarosite to be Cu > Zn > Co ~ Ni ~ Mn > Cd, which is the same as the ease of hydrolysis.

Decreases in γ_{eff} are recorded for the $M_K^{\bullet} + V_K^{/}$ mechanism (Table 4), suggesting that the surfaces become more stable with increasing substitution of 2+ metal cations on the K sites. Positive U_{sol} values suggest, however, that impurity incorporation from solution via this mechanism at the pH of the zero point of charge of jarosite is not favored (except for Cu on the 012-S2 surface when the defect is unbound; Table 9). Our surface calculations agree well with those carried out for bulk jarosite by Smith et al. (2006a), who also found that substitutions at K sites would be limited due to endothermic solution energies and structural considerations. There is little evidence that Cu, Zn or Cd substitute at the K-site in natural or synthetic jarosite-group minerals, despite the fact that other divalent ions (e.g., Ca^{2+} and Pb^{2+}) are known to do so (Scott, 1987; Dutrizac and Jambor, 2000). This may be a real feature or the fact that no study, to the authors' knowledge, has attempted to prove or disprove this. In any case, the amount of substitution is likely to be limited, due to the large size of the K ion (1.64 Å, CN=12;

Shannon, 1976) compared to that of Cd (1.31 Å, CN=12; no data are available for Cu or Zn for CN=12; Shannon, 1976), and because incorporation of these impurities leads to considerable distortion of the surfaces (e.g., Fig. 1). Also, because the defects are coupled, increasing their numbers would create so many defects on the mineral surfaces that they would be completely destabilized. All of this is confirmed by studies of natural and synthetic jarosite-group minerals: Dutrizac et al. (1996) demonstrated that synthetic jarosite-group minerals could take up only < 0.5 wt. % Cd, even when they were made with Cd-rich solutions (up to 40 g L^{-1} Cd). The maximum content of Zn in jarosite is 2.1-2.5 wt.% (Dutrizac, 1984; Scott, 1987), and of Cu in natrojarosite is < 2 wt.% Cu.

The calculations suggest that incorporation via the $M'_{Fe} + V^{\bullet}_{OH}$ and $M^{\bullet}_{K} + M'_{Fe}$ mechanisms is unfavorable. Within the alunite supergroup, Cu^{2+} and Zn^{2+} substitution for Fe^{3+} is observed mainly in natural and synthetic beaverite minerals [$Pb(Fe,Cu,Zn)_3(SO_4)_2(OH)_6$] (Dutrizac and Jambor, 2000; Hudson-Edwards et al., 2008), where the charge is balanced by incorporation of Pb^{2+} on the A-site rather than an OH^- vacancy, as in our calculations. Other studies have shown that Zn^{2+} fills unoccupied trigonal bipyramidal sites previously unreported in alunite-type structures (Grey et al., 2008, 2009). There are no studies that have demonstrated coupled substitution of 2+ metal cations on both the K and Fe sites in natural or synthetic jarosite-group minerals. A possible mechanism for incorporating the 2+ metal cations in the B-site in jarosite might be by growing a new layer of jarosite or goethite after incorporating the impurity, as predicted for bulk jarosite by Smith et al. (2006a). Dynamic experiments using atomic force microscopy, for example, could confirm whether or not this was a viable process.

Overall, our data suggest that incorporation of impurities is most favored on the 001-S3 and 012-S2 surfaces, although incorporation via the $M^{\bullet}_{K} + V'_{K}$ and $M'_{Fe} + V^{\bullet}_{OH}$ mechanisms on 012-S2 results in considerable distortion of the surface. Substitutions on the 012-S1, 001-S1 and especially, 001-S2, surfaces are less favorable and promote unstable surfaces. This may be one explanation why faster growing (001) faces disappear in favor of more stable (012) faces (Becker and Gasharova, 2001),

in that new growth will take place to cover these unstable surfaces and move the impurities into the bulk structure.

4. CONCLUSIONS

We have used atomistic simulation methods to determine the mechanisms of uptake and incorporation of Al, Cd, Cu and Zn on jarosite (012) and (001) surfaces. The pure (001) surfaces have lower calculated energies than the (012) surfaces, suggesting that jarosite crystals should be mostly bound by the (001) surface. That this is not commonly observed (e.g., Becker and Gasharova, 2001; Gasharova et al., 2005) could be due to several factors. The controls on morphology during growth will be governed by fluid composition, pH and other conditions. There may also be competition between thermodynamic and kinetic controls on crystal growth. Our calculations assume thermodynamic equilibrium and do not include the effects of solution on the surface. Any one, or combination of the above factors could be responsible for our results. We are conscious of these approximations and hope to be able to develop a model of the surface under water. In many cases, the predicted equilibrium morphology can be different from those observed, even where water is included in the simulation, and even for those surfaces calculated *ab initio*.

The results of the surface metal ion incorporation simulations show that substitution of Al at Fe sites is favorable and leads to stabilization of the surfaces. Although substitution of the 2+ metal cations at the K surfaces balanced by a K vacancy leads to stabilization of 012-S2 and 001-S1 surfaces, these substitutions will likely be limited due to endothermic solution energies and structural factors, as Smith et al. (2006a) found for these substitutions in for bulk jarosite. Substitution of Cd, Cu and Zn at Fe sites, coupled with OH vacancies providing charge-neutrality, and coupled substitutions at both K and Fe sites, are predicted to be unlikely due to endothermic solution energies and large increases in surface energies (especially for the (001) surfaces), which will make the surfaces highly distorted and unstable,

and promote rapid growth. Our work indicates that surface structure influences the uptake of impurities, thus agreeing with other work on environmentally-important minerals such as sphalerite (Wright, 2009).

Acknowledgements. KH-E and KW acknowledge the Royal Society and the Australian Research Council, respectively, for funding. We also thank the iVEC (interactive Virtual Environment Centre) for provision of computational resources, and Julian D. Gale for invaluable discussions and advice. Finally, we thank the two anonymous reviewers and associate editor David Vaughan for their insightful comments that improved the manuscript.

REFERENCES

Allan, N. L., Rohl, A. L., Gay, D. H., Catlow, C. R. A., Davey, R. J. and Mackrodt, W. C. (1993) Calculated bulk and surface properties of sulfates. *Faraday Disc*. **95**, 273-280.

Alpers, C. N., Rye, R. O., Nordstrom, D. K., White, L. D. and King Bi-Shia (1992) Chemical, crystallographic and stable isotopic properties of alunite and jarosite from acid-hypersaline Australian lakes. *Chem. Geol*. **96**, 203-226.

Baron, D. and Palmer, C.D. (1996) Solubility of jarosite at 4-35°C. *Geochim. Cosmochim. Acta* **60**, 185-195.

Becker, U. and Gasharova, B. (2001) AFM observations and simulations of jarosite growth at the molecular scale: probing the basis for incorporation of foreign ions into jarosite as a storage mineral. *Phys. Chem. Miner*. **28**, 545-556.

Benison, K. C., Bowen, B. B., Oboh-Ikuenobe, F. E., Jagniecki, E. A., LaClair, D. A., Story, S. L., Mormile, M. R. and Hong, B. Y. (2007) Sedimentology of acid saline lakes in southern Western Australia: Newly described processes and products of an extreme environment. *J. Sed. Res*. **77**, 366-388.

Brophy G. P. and Sheridan M. F. (1965) Sulfate studies IV: The jarosite-natrojarosite-hydronium jarosite solid solution series. *Am. Mineral*. **50**, 1595-1607.

Brophy, G. P., Scott, E. S. and Snellgrove, R. A. (1962) Sulphate studies II. Solid solution between alunite and jarosite. *Am. Mineral*. **47**, 112-126.

Catlow, C. R. A. (2003) Computer modelling of materials: an introduction. In: Catlow, C. R. A., Kotomin, E. (eds.) *Computational Materials Science*, NATO Science Series. IOS Press, Amsterdam.

Catlow, C. R. A. and Mackrodt, W. C., Eds. (1982) *Computer Simulation of Solids*. Springer-Verlag, Berlin, 320 p.

Dutrizac, J. E. (1984) The behaviour of impurities during jarosite precipitation. In: Bautista, R. G. (Ed.)

Hydrometallurgical Process Fundamentals. Plenum Press, New York, pp. 125-169.

Dutrizac, J.E. & Dinardo, O. (1983) The co-precipitation of copper and zinc with lead jarosite. *Hydrometallurgy* **11**, 61-78.

Dutrizac J. E. and Jambor J. L. (2000) Jarosites and their applications in hydrometallurgy. In *Sulfate Minerals: Crystallography, Geochemistry, and Environmental Significance*, vol. 40 (eds. C. N. Alpers, J. L. Jambor and D. K. Nordstrom). Mineralogical Society of America, pp. 405-452.

Dutrizac, J. E. and Kaiman, S. (1976) Synthesis and properties of jarosite-type compounds. *Can. Mineral*. **14**, 151-158.

Dutrizac, J. E., Hardy, D. J. and Chen, T.T. (1996) The behaviour of cadmium during jarosite precipitation. *Hydrometallurgy* **41**, 269-285.

Fleming, S. and Rohl, A. (2005) GDIS: a visualization program for molecular and periodic systems. *Z. Kryst.* **220**, 580-584.

Gale, J. D. and Rohl, A. L. (2003) The General Utility Lattice Program (GULP). *Molecular Simulations* **29**, 291-341.

Gasharova B., Göttlicher J., and Becker U. (2005) Dissolution at the surface of jarosite: an in-situ AFM study. *Chem. Geol*. **215**, 499-516.

Gräfe, M., Beattie, D. A., Smith, E., Skinner, W. M. and Singh, B. (2008) Copper and arsenate co-sorption at the mineral-water interfaces of goethite and jarosite. *J. Colloid Int. Sci*. **322**, 399-413.

Grey, I.E., Mumme, W.G., Bordet, P. and Mills, S. (2008) A new crystal-chemical variation of the alunite-type structure in monoclinic $PbZn_{0.5}Fe_3(ASO_4)_2(OH)_6$. *Can. Mineral*. **46**, 1355-1364.

Grey, I.E., Mumme, W.G., Mills, S.J., Birch, W.D. and Wilson, N.C. (2009) The crystal chemical role of Zn in alunite-type minerals: structure refinements for kintoreite and zincian kintoreite. *Am. Mineral*. **94**, 676-683.

Hawthorne F. C., Krivovichev S. V., and Burns, P. C. (2000) The crystal chemistry of sulphate minerals. In *Sulfate Minerals: Crystallography, Geochemistry, and Environmental Significance*, vol.

40 (eds. C. N. Alpers, J. L. Jambor and D. K. Nordstrom). Mineralogical Society of America, pp. 1-112.

Hudson-Edwards, K. A. Schell, C. and Macklin, M. G. (1999) Mineralogy and geochemistry of alluvium contaminated by metal mining in the Rio Tinto area, southwest Spain. *Appl. Geochem*. **14**, 55-70.

Hudson-Edwards, K. A., Smith, A. M. L., Dubbin, W. E., Bennett, A. J., Murphy, P. J. and Wright, K. (2008) Comparison of the structures of natural and synthetic Pb-Cu-jarosite-type compounds. *Eur. J. Mineral.* **20**, 241-252.

Jambor, J. L. (1999) Nomenclature of the alunite supergroup. *Can. Mineral*. **37**, 1323-1341.

Jiang, H. and Lawson, F. (2006) Reaction mechanism for the formation of ammonium jarosite. *Hydrometallurgy* **82**, 195-198.

Klingelhofer, G., Morris, R. V., Bernhardt, B., Schroder, C., Rodionov, D. S., de Souza, P. A., Yen, A., Gellert, R., Evlanov, E. N., Zubkov, B., Foh, J., Bonnes, U., Kankeleit, E., Gutlich, P., Ming, D. W., Renz, F., Wdowiak, T., Squyres, S. W. and Arvidson, R. E. (2004) Jarosite and hematite at Meridiani Planum from Opportunity's Mossbauer spectrometer. *Science* **306**, 1740-1745.

Kröger, F.A. (1972) The chemistry of imperfect crystals. North Holland, Amsterdam.

Kubisz J. (1964) A study of minerals in the alunite-jarosite group. *Polska Akad. Nauk. Prace Geol*. **22**, 1-93.

Kubisz J. (1970) Studies on synthetic alkali-hydronium jarosites. I. Synthesis of jarosite and natrojarosite. *Mineralogia Polonica* **1**, 47-57.

Marcus, Y. (1991) Thermodynamics of solvation of ions. *J. Chem. Soc. Faraday Trans*. **87**, 2995-2999.

Martinez-Frías, J., Lunar, R., Rodríguez-Losada, J. A., Delgado, A. and Rull, F. (2004) The volcanism-related multistage hydrothermal system of El Jaroso (SE Spain): Implications for the exploration of Mars. *Earth Planets Space* **56**, 5-8.

Majzlan, J., Speziale, S., Duffy, T. S., Burns, P. C. (2006) Single-crystal elastic properties of alunite,

$KAl_3(SO_4)_2(OH)_6$. *Phys. Chem. Mineral*. **33**, 567-573.

Menchetti, S. and Sabelli, C. (1976) Crystal chemistry of the alunite series; crystal structure refinement of alunite and synthetic jarosite. *Neues Jahr. Miner. Monatshefte* **9**, 406-417.

Nordstrom, D. K. and May, H. M. (1996) Aqueous equilibrium data for mononuclear aluminum species. In Sposito, G. (Ed.) *The Environmental Chemistry of Aluminum, 2nd edition*. CRC Press / Lesis Publishers, Boca Raton, Florida, pp. 39-80.

Saul, P., Catlow, C. R. A., and Kendrick J. (1985) Theoretical-studies of protons in sodium-hydroxide. *Phil. Mag. B – Phys. Condensed Matter Statistical Mechanics Electronic Optical and Magnetic Properties* **51**, 107-117.

Scott, K. M. (1987) Solid solution in, and classification of, gossan-derived members of the alunite-jarosite family, northwest Queensland, Australia. *Am. Mineral*. **72**, 178-187.

Shannon, R. D. (1976) Revised effective ionic radii and systematic studies of interatomic distances in halides and chalcogenides. *Acta Crystallogr*. **A32**, 751-767.

Smith, A. M. L., Hudson-Edwards, K. A., Dubbin, W. E., Wright, K. (2006a) Defects and impurities in jarosite: A computer simulation study. *Appl. Geochem*. **21**, 1251-1258.

Smith, A. M. L., Hudson-Edwards, K. A., Dubbin, W. E. and Wright, K. (2006b) Dissolution of jarosite [$KFe_3(SO_4)_2(OH)_6$] at pH 2 and 8: Insights from batch experiments and computational modelling. *Geochim. Cosmochim. Acta* **70**, 608-621.

Stoffregen R. E., Alpers C. N., and Jambor J. L. (2000) Alunite-jarosite crystallography, thermodynamics and geochronology. In *Sulfate Minerals: Crystallography, Geochemistry, and Environmental Significance*, vol. 40 (eds. C. N. Alpers, J. L. Jambor and D. K. Nordstrom). Mineralogical Society of America, pp. 453-479.

Tasker P. W. (1979) Stability of ionic crystal surfaces. *J. Chem. Phys. C: Solid State Phys.* **12**, 4977-4984.

Timms, N. E., Li, J. and Reddy, S. M. (2009) Quantitative microstructural characterization of

natrojarosite scale formed during high-pressure acid leaching of lateritic nickel ore. *Am. Mineral*. **94**, 1111-1119.

Wallert, A. (1995) Unusual pigments on a Greek marble basin. *Studies in Conservation* **40**, 177-188.

Welch, S. A., Christy, A. G., Kirste, D., Beavis, S. B. and Beavis, F. (2007) Jarosite dissolution I - trace cation flux in acid sulfate soils. *Chem. Geol*. **245**, 183-197.

Woodley, S. M., Battle, P. D., Gale, J. D. and Catlow, C. R. A. (1999) The prediction of inorganic crystal structures using a genetic algorithm and energy minimisation. *Phys. Chem. Chem. Phys*. **1**, 2535-2542.

Wright, K. (2009) The incorporation of cadmium, manganese and ferrous iron in sphalerite: insights from computer simulations. *Can. Mineral*. **47**, 615-623.

Wright, K., Hudson-Edwards, K. A., Smith, A. M. L. and Dubbin, W. E. (2008) Computer simulation studies on the mechanisms of toxic element incorporation in jarosite. *AusIMM 9th International Congress for Applied Mineralogy (ICAM)*, pp. 369-374.

FIGURES

Figure 1. Examples of surface substitutions.

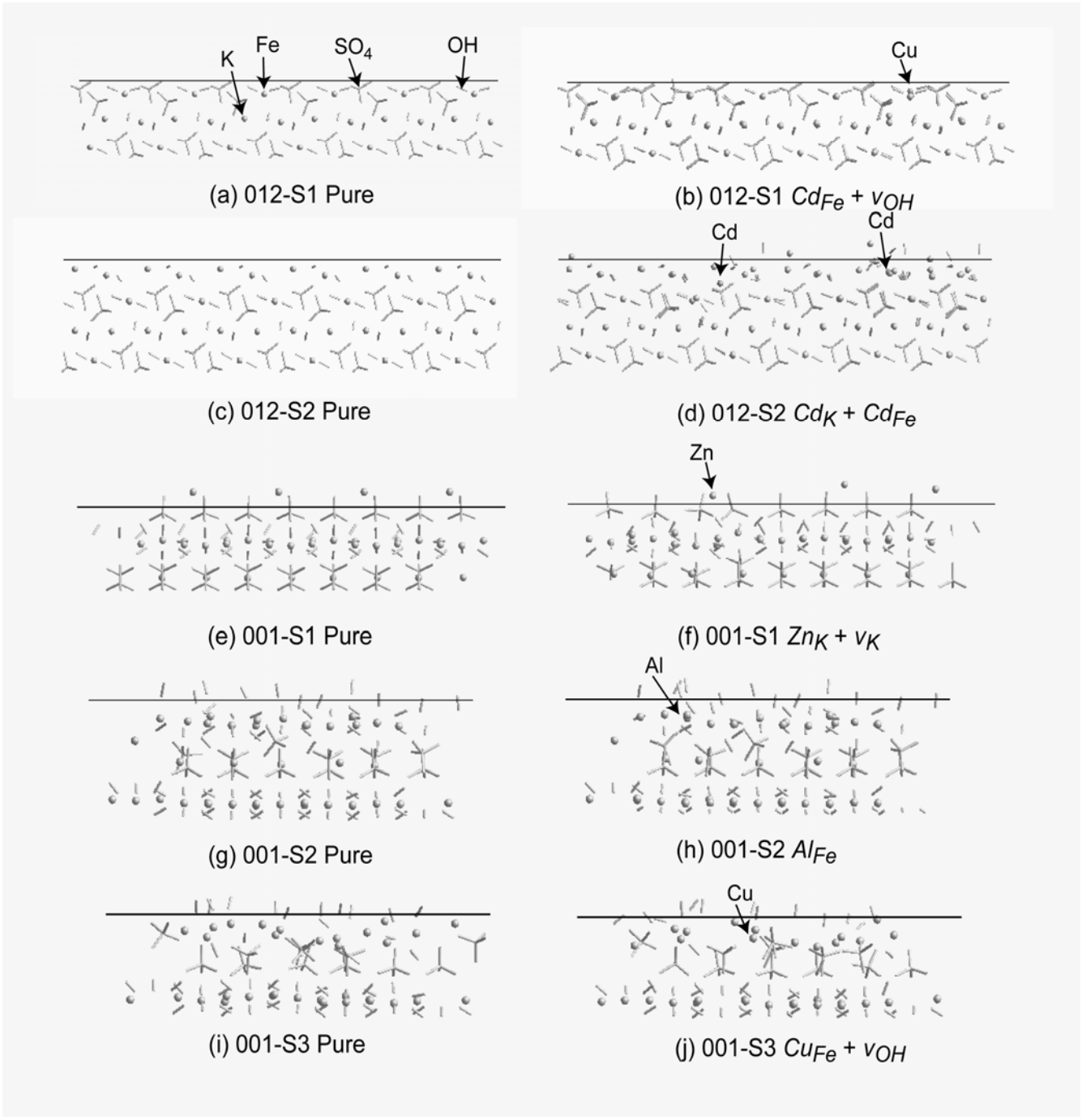

Tables

Table 1. Potential parameters used to model end-member jarosite and incorporate impurities.

End-member jarosite model				
Buckingham	A (eV)	ρ (Å)	C (eV Å^6)	Reference
K-O1	1080.992	0.3000	0.00	a
K-O3	1250.666	0.3000	0.00	a
Fe-O1	987.446	0.2297	0.00	a
Fe-O3	1375.048	0.2297	0.00	a
O1-O1	103585.02	0.20000	25.98	b
O1-O3	103585.02	0.20000	25.98	b
O3-O3	103585.02	0.20000	25.98	b
Morse intra bond	D_{ij} (eV)	α (Å^{-1})	r_0 (Å)	
S-O1	5.0	1.2	1.515	d
H-O2	7.0525	2.1986	0.9685	a
Buckingham interpotential	A (eV)	ρ (Å)	C (eV Å^6)	
H-O	161.844	0.2500	0.000	a
Three body intrapotential	k_3 (eV rad^{-2})	Θ (º)		
O1-S-O1	15.0	109.47		d
Potential parameters for Al, Cd, Cu and Zn impurities				
Buckingham	A (eV)	ρ (Å)	C (eV Å^6)	Reference
Al-O1	576.113	0.2291	0.00	a
Al-O3	1038.106	0.2291	0.00	a
Cd-O1	364.868	0.35	0.00	c
Cd-O3	868.30	0.35	0.00	c
Cu-O1	700.1988	0.30	0.00	c
Cu-O3	1188.67	0.30	0.00	c
Zn-O1	294.126	0.3372	0.00	c
Zn-O3	499.60	0.3595	0.00	c

References: a, fitted, this study; b, Smith et al. (2006a); c, Woodley et al. (1999); d, Allan et al. (1993); d, Saul et al. (1985). O1 and O2 represent the sulfate oxygens (q = -0.84) and O3 the hydroxyl oxygen (q = -1.426). The short range Buckingham potential cutoff was set to 10 Å for all elements except Al, for which the cutoff was set to 20 Å.

Table 2. Comparison of experimental (Menchetti and Sabelli, 1976) and calculated cell parameters and interatomic distances and angles for jarosite. Calculated cell parameters for jarosite from Smith et al. (2006a) are included for comparison. All distances in angstroms (Å).

	Experimental (Menchetti and Sabelli, 1976)	Calculated (this study) (% difference)	Calculated (Smith et al., 2006a, b) (% difference)
a	7.315	7.317 (0.03)	7.443 (1.75)
b	7.315	7.317 (0.03)	7.443 (1.75)
c	17.224	17.225 (0.006)	17.497 (1.58)
Vol ($Å^3$)	798.17	798.78 (0.08)	839.40 (5.17)
a/c	0.4247	0.4248 (0.02)	0.4254 (0.16)
		Bond lengths	
S-O	1.465	1.401	1.466
S-O×3	1.481	1.428	1.543
K-O×6	2.828	2.847	2.941
K-O×6	2.978	3.050	2.981
Fe-O×2	2.058	2.078	2.192
Fe-O×4	1.975	1.970	1.988
O-H	0.750	1.022	0.882
O-H...O	2.220	2.297	2.096
O-H...O	2.942	2.981	2.939
		Bond angles	
O-Fe-O (º)	91.2	91.72	90.19
O-Fe-O (º)	88.8	88.28	89.81
O-Fe-O (º)	88.8	88.28	88.92
O-Fe-O (º)	91.2	91.72	91.08
Fe-O-Fe (º)	135	136.49	138.73

Table 3. Calculated unrelaxed and relaxed jarosite (012) and (001) surface energies.

Face	Composition	Surface Area (Å)	Unrelaxed Surface Energy ($J\ m^{-2}$)	Relaxed Surface Energy ($J\ m^{-2}$)	Energy Relaxed Surface ($kJ\ mol^{-1}$)
012-S1	$[Fe_2(SO_4)_2(OH)_2]^0$	938.94	1.57	1.19	-2786300
012-S2	$[KFe(OH)_4]^0$	938.94	1.57	0.99	-2787430
001-S1	$[K(SO_4)_2]^{3-}$	370.99	0.78	0.43	-2487910
001-S2	$[Fe_5(OH)_{12}]^{3+}$	278.24	7.43	1.01	-1853800
001-S3	$[Fe_3(OH)_3]^{6+}$	278.24	12.20	1.08	-1845680

Table 4. Calculated effective surface energies for unbound (UB) and bound (B) impurity substitutions.

Defect	012-S1		012-S2		001-S1		001-S2		001-S3	
	γ_{eff} (J m^{-2})		γ_{eff} (J m^{-2})		γ_{eff} (J m^{-2})		γ_{eff} (J m^{-2})		γ_{eff} (J m^{-2})	
Al_{Fe}^{x}	1.14		0.93				0.83		0.88	
	UB	B	UB	B	UB	B	UB	B	UB	B
$Cd_K^{\bullet} + V_K^{/}$			0.82	0.82	0.91	0.12			0.60	0.62
$Cu_K^{\bullet} + V_K^{/}$			0.74	0.77	0.89	0.08			0.52	0.54
$Zn_K^{\bullet} + V_K^{/}$			0.78	0.81	0.90	0.11			0.57	0.59
$Cd_{Fe}^{/} + V_{OH}^{\bullet}$	1.84	1.90	1.64	1.58			3.30	3.18	3.12	3.28
$Cu_{Fe}^{/} + V_{OH}^{\bullet}$	1.81	1.87	1.65	1.61			3.09	3.08	2.68	2.63
$Zn_{Fe}^{/} + V_{OH}^{\bullet}$	1.82	1.90	1.60	1.62			3.14	3.14	2.76	2.67
$Cd_K^{\bullet} + Cd_{Fe}^{/}$			1.19	1.18					1.76	1.78
$Cu_K^{\bullet} + Cu_{Fe}^{/}$			1.10	1.13					1.56	1.61
$Zn_K^{\bullet} + Zn_{Fe}^{/}$			1.15	1.16					1.69	1.70

Table 5. Calculated substitution energies (U_{subs}) for unbound (UB) and bound (B) substitutions.

Defect	012-S1		012-S2		001-S1		001-S2		001-S3	
	U_{Subs} (kJ mol^{-1})		U_{Subs} (kJ mol^{-1})		U_{Subs} (kJ mol^{-1})		U_{Subs} (kJ mol^{-1})		U_{Subs} (kJ mol^{-1})	
Al_{Fe}^{x}	-313		-339				–315		-349	
	UB	B	UB	B	UB	B	UB	B	UB	B
$Cd_K^{\bullet} + V_K^{/}$			-982	-1005	-498	-513			-800	-764
$Cu_K^{\bullet} + V_K^{/}$			-1445	-1259	-574	-581			-942	-899
$Zn_K^{\bullet} + V_K^{/}$			-1223	-1065	-543	-542			-862	-822
$Cd_{Fe}^{/} + V_{OH}^{\bullet}$	3648	3980	3662	3319			3824	3646	3418	3688
$Cu_{Fe}^{/} + V_{OH}^{\bullet}$	3484	3819	3690	3456			3476	3465	2675	2604
$Zn_{Fe}^{/} + V_{OH}^{\bullet}$	3525	3908	3449	3545			3571	3567	2803	2663
$Cd_K^{\bullet} + Cd_{Fe}^{/}$			1098	1075					1138	1174
$Cu_K^{\bullet} + Cu_{Fe}^{/}$			575	767					803	895
$Zn_K^{\bullet} + Zn_{Fe}^{/}$			852	927					1022	1040

Table 6. Coordination and bond length changes on introduction of Al at an Fe site in jarosite.

Surface	M(III) coordination	O-Fe Mean Å	O-Al Mean Å
012-S1	2 × O1	1.991	1.819
	3 × O2	1.948	1.879
012-S2	1 × O1	1.994	1.780
	4 × O2	1.928	1.860
001-S2	1 × O1	2.090	1.998
	5 × O2	1.997	1.940

Table 7. Calculated binding energies (U_{Bind}) for jarosite (012) and (001) surface substitutions.

Defect	012-S1 U_{Bind} (kJ mol^{-1})	012-S2 U_{Bind} (kJ mol^{-1})	001-S1 U_{Bind} (kJ mol^{-1})	001-S2 U_{Bind} (kJ mol^{-1})	001-S3 U_{Bind} (kJ mol^{-1})
$Cd_K^{\bullet} + V_K^{/}$		-22	-15		36
$Cu_K^{\bullet} + V_K^{/}$		186	-7		42
$Zn_K^{\bullet} + V_K^{/}$		158	0		40
$Cd_{Fe}^{/} + V_{OH}^{\bullet}$	332	-344		-178	270
$Cu_{Fe}^{/} + V_{OH}^{\bullet}$	335	-235		-10	-72
$Zn_{Fe}^{/} + V_{OH}^{\bullet}$	383	96		-4	-140
$Cd_K^{\bullet} + Cd_{Fe}^{/}$		-23			37
$Cu_K^{\bullet} + Cu_{Fe}^{/}$		193			92
$Zn_K^{\bullet} + Zn_{Fe}^{/}$		75			18

Table 8. Solution reactions for incorporation of impurity ions from solution into jarosite surfaces. M=Cd, Cu or Zn.

Defect	Solution Reaction	Solution Reaction Number
Al_{Fe}^{x}	$Fe_{Fe} + \mathrm{Al^{3+}_{(aq)}} > Al_{Fe} + \mathrm{Fe^{3+}_{(aq)}}$	1
$M_{K}^{\bullet} + V_{K}^{/}$	$2\ K_K + \mathrm{M^{2+}_{(aq)}} > M_K + 2\ \mathrm{K^{+}_{(aq)}}$	2
$M_{Fe}^{/} + V_{OH}^{\bullet}$	$Fe_{Fe} + \mathrm{M^{2+}_{(aq)}} + OH_{OH} > M_{Fe} + \mathrm{Fe^{3+}_{(aq)}} + \mathrm{OH^{-}_{(aq)}}$	3
$M_{K}^{\bullet} + M_{Fe}^{/}$	$K_K + Fe_{Fe} + 2\mathrm{M^{2+}_{(aq)}} > M_K + M_{Fe} + \mathrm{Fe^{3+}_{(aq)}} + \mathrm{K^{+}_{(aq)}}$	4

Table 9. Calculated segregation energies with respect to aqueous solution (U_{Sol}, in kJ mol^{-1}) for unbound (UB) and bound (B) defect substitutions.

Defect	Reaction (Table 8)	012-S1		012-S2		001-S1		001-S2		001-S3	
		U_{Sol} (kJ mol^{-1})		U_{Sol} (kJ mol^{-1})		U_{Sol} (kJ mol^{-1})		U_{Sol} (kJ mol^{-1})		U_{Sol} (kJ mol^{-1})	
Al_{Fe}^{x}	1	-52.6		-78.7				-54.6		-89.3	
		UB	B	UB	B	UB	B	UB	B	UB	B
$Cd_K^{\bullet} + V_K^{/}$	2			161	160	667	652			365	401
$Cu_K^{\bullet} + V_K^{/}$	2			-24.4	161	846	839			478	521
$Zn_K^{\bullet} + V_K^{/}$	2			142	300	822	822			503	543
$Cd_{Fe}^{/} + V_{OH}^{\bullet}$	3	2443	2776	2458	2115			2620	2442	2214	2484
$Cu_{Fe}^{/} + V_{OH}^{\bullet}$	3	2789	3125	2996	2761			2782	2771	1981	1909
$Zn_{Fe}^{/} + V_{OH}^{\bullet}$	3	2721	3104	2645	2741			2766	2762	1999	1860
$Cd_K^{\bullet} + Cd_{Fe}^{/}$	4			48.3	24.9					87.6	125
$Cu_K^{\bullet} + Cu_{Fe}^{/}$	4			24.1	227					263	355
$Zn_K^{\bullet} + Zn_{Fe}^{/}$	4			202	277					372	390